Materials Advances

ROYAL SOCIETY OF CHEMISTRY

PAPER

View Article Online
View Journal | View Issue

Cite this: *Mater. Adv.*, 2026, 7, 2982

High thermoelectric power conversion efficiency of an earth-abundant Janus silicon oxy-sulfide monolayer: a first-principles study

Zakariae Darhi, *[a] Mounaim Bencheikh,[a] Ravindra Pandey[b] and Larbi El Farh[a]

Received 10th November 2025,
Accepted 13th January 2026

DOI: 10.1039/d5ma01306b

rsc.li/materials-advances

The tunable properties of Janus monolayers, along with advances in their synthesis, make these low-symmetry materials excellent candidates for thermoelectric power generation. In this study, we systematically investigate the electronic and thermal properties of the Janus silicon oxy-sulfide monolayer. The results based on density functional theory reveal that the monolayer is stable. It exhibits a tunable direct band gap and strong covalent bonding. Its ultralow lattice thermal conductivity (<0.38 W mK^{-1} at 300 K) is attributed to the broken phonon selection rule for phonon–phonon scattering and a high level of anharmonicity, as reflected in the large Grüneisen parameter. Furthermore, the inclusion of four-phonon scattering introduces additional anharmonic phonon–phonon interactions, leading to a 50% reduction in lattice thermal conductivity, which results in a significant enhancement of the thermoelectric figure of merit of 3.62 and power conversion efficiency of 30.89% for the n-type Janus SiOS monolayer, highlighting its potential for efficient waste heat recovery applications.

Introduction

The rapid global population growth is driving the focus toward sustainable and low-cost energy sources to meet global needs without further dependence on oil, natural gas, or coal.[1] Despite progress in renewables, a large portion of primary energy, approximately 63%, is lost as waste heat during generation and transfer processes in the transportation, industrial, and residential sectors.[2,3] Therefore, improving energy efficiency through waste heat recovery technologies, such as thermoelectricity, would be highly beneficial for both environmental protection and economic development.[4] The formula derived by Altenkirch evaluates the thermoelectric (TE) conversion efficiency of a device, and was later optimized by Abram Ioffe in 1957:[5]

$$\eta(\%) = \frac{T_{\text{hot}} - T_{\text{cold}}}{T_{\text{hot}}} \cdot \frac{\sqrt{1+\overline{ZT}} - 1}{\sqrt{1+\overline{ZT}} + T_{\text{cold}}/T_{\text{hot}}} \quad (1)$$

where T_{hot} and T_{cold} are the hot- and cold-side temperatures, respectively. At the material level, TE efficiency is characterized by the Figure of Merit, $ZT = S^2\sigma T/\kappa$, where S, σ, and κ are the Seebeck coefficient, electrical conductivity, and overall thermal conductivity, respectively.

The advent of low-dimensional materials following the discovery of graphene in 2004 has redirected attention toward Janus materials, whose asymmetric structures give rise to unique properties.[6,7] Janus monolayers have been proposed for various applications, such as toxic gas detection,[8] optoelectronics,[9,10] thermoelectric devices,[11–14] and photocatalysis.[15] Furthermore, Janus monolayers have recently attracted increasing interest for thermoelectric energy conversion; their inherent asymmetry reduces phonon lifetimes, increases phonon scattering, and diminishes contributions from flexural (ZA) modes to heat transport. Consequently, the lattice thermal conductivity is suppressed while preserving electronic transport. Similar effects have been found for systematically reported Janus monolayers.[16–19]

Along with the intrinsic benefits of Janus features, our material focus is based on the abundance and non-toxicity of these elements. Additionally, the thermo-chemical stability of silicon dioxide (SiO_2) and silicon disulfide (SiS_2) is well-established, both of which have been widely characterized by many experimentalists.[20–24] We propose a new Janus SiOS monolayer. This structure combines the characteristics of the parent materials, offering a sustainable and environmentally friendly candidate for thermoelectric energy conversion. Herein, we present a detailed first-principles study of the structural, electronic, transport, and thermal properties of a new Janus Silicon Oxy-Sulfide (SiOS) monolayer.

[a] *Mohammed First University, Faculty of Sciences, Department of Physics, Oujda 60000, Morocco. E-mail: zakariae.darhi@ump.ac.ma*
[b] *Michigan Technological University, Department of Physics, 1400 Townsend Drive, Houghton, MI 49931, USA*

Computational details

Density functional theory (DFT) calculations were performed using the Vienna *Ab Initio* Simulation Package (VASP).[25] The exchange–correlation interactions were treated within the generalized gradient approximation (GGA).[26] We chose a 15 × 15 × 1 *k*-point mesh to sample the first Brillouin zone under the Monkhorst–Pack scheme[27] for both structural relaxations and electronic structure calculations, with convergence criteria of 10^{-8} eV for total energy and 10^{-3} eV Å^{-1} for atomic forces, and a kinetic energy cutoff of 600 eV. van der Waals (vdW) interactions were incorporated using the DFT-D3 method.[28] To minimize spurious periodic interactions, we extended the *z*-axis by 20 Å.

By solving the Boltzmann transport equation (BTE) for electrons, the electronic transport factors are calculated under the relaxation time and rigid band approximations as implemented in the BoltzTraP2 code,[29] using Heyd–Scuseria–Ernzerhof (HSE06)[30] band structures sampled on a fine *q*-mesh of 150 × 150 × 1. Then, we considered the three main mechanisms of scattering, including the elastic ionized impurity scattering (IMP), the elastic acoustic deformation potential scattering (ADP), and the inelastic polar optical phonon scattering (POP), to calculate the electronic relaxation time using first principles for carrier scattering as implemented in the AMSET package[31] and the Matthiessen rule.[32] Within the Born approximation, the scattering rate ($\tau_{i\boldsymbol{k}\rightarrow j\boldsymbol{k}+\boldsymbol{q}}^{-1}$) for an electron from an initial state $i\boldsymbol{k}$, to the final state $i\boldsymbol{k}+\boldsymbol{q}$ is described using Fermi's golden rule:[33,34]

$$\frac{1}{\tau_{ik\rightarrow jk+q}} = \frac{2\pi}{\hbar}\delta\left(E_{ik} - E_{jk+q}\right)\left|g_{ij}(k,q)\right|^2 \qquad (2)$$

where i and j are band indices, k and q are the wave vectors, $\hbar$ is the reduced Planck's constant, E is the electron energy, and $g_{ij}(k,q)$ is the coupling matrix element. The detailed input parameters used to evaluate these scattering rates (such as elastic constants (C_{ij}), band gap energy, acoustic deformation potential (E_d) optical polar phonon (pop) frequency ($\hbar\omega_{pop}$), static (ε_s) and high-frequency (ε_∞) dielectric constants) are obtained from DFT calculations and are analyzed throughout the paper or provided in the SI.

The lattice thermal conductivity was calculated by solving iteratively the phonon Boltzmann transport equation (BTE) using the ShengBTE package[35] and, within the relaxation time approximation (RTA), using the FourPhonon code.[36] Second-order interatomic force constants (IFCs) were obtained using density-functional perturbation theory (DFPT)[37] as implemented in the Phonopy package,[38] employing a 6 × 6 × 1 supercell and a 3 × 3 × 1 *k*-point grid. Subsequently, the finite-displacement method implemented in ALAMODE[39] was used to extract third- and fourth-order IFCs, considering interactions up to the eighth and sixth nearest neighbours, respectively, within a 4 × 4 × 1 supercell. The harmonic phonon spectra were further corrected using the HiPhive framework[40] to enforce the rotational invariance condition. Isotope and boundary scattering were included to account for natural mass disorder and finite-size effects. In addition, the non-analytical term correction (NAC) was applied to properly describe long-range Coulomb interactions and LO-TO splitting in the Janus SiOS monolayer, using a converged dense *q*-point mesh of 30 × 30 × 1. As the harmonic phonon dispersion exhibits low-frequency soft-mode characteristics in the ZA branch near the K point (Fig. S1), temperature-induced phonon renormalization effects were further considered using the self-consistent phonon (SCPH) method as implemented in ALAMODE. In this approach, quartic anharmonic force constants were employed to obtain temperature-dependent renormalized phonon frequencies.[41]

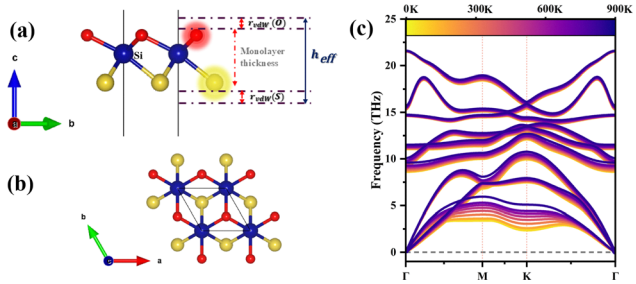

Fig. 1 (a) Top and (b) side views, and (c) anharmonic phonon normalized spectra using SCPH theory of the Janus SiOS monolayer.

Ab initio molecular dynamics (AIMD) simulations were performed at 300 K using a 5 × 5 × 1 supercell based on the canonical ensemble (NVT), with a time step of 1 fs and a total simulation time of 10 ps.[42,43] The convergence tests are presented in the SI (Fig. S4).

Since the lattice thermal conductivity (κ_{ph}), electronic thermal conductivity (κ_e), and electrical conductivity (σ) are inversely proportional to the volume, for normalization, we multiplied these parameters by z/h_{eff}, where z is the vacuum in the *z*-axis and h_{eff} is the effective thickness of the monolayer, defined as the sum of the interplanar distance between the top and bottom atomic layers and the van der Waals radii of the surface atoms r_{vdW} (O,S)[44] as shown in Fig. 1(b).

Results and discussion

Structure and stability

We constructed the monolayer using a 2D silica-like sheet within the $P\bar{3}m1$ (No. 162) space group, in which one of the oxygen layers was replaced by a sulfur atom (top O → S), yielding a Janus SiOS monolayer. The optimized structure adopts a van der Waals layered hexagonal configuration with reduced symmetry, belonging to the $P3m1$ (No. 153) space

Table 1 Calculated lattice parameters, effective thickness (h_{eff}), interatomic distances (d), and cohesive energy (E_{coh}) of Janus silicon oxy-sulfide monolayer SiOS

	d (Å)				
$a = b$ (Å)	Si–S	Si–O	h_{eff} (Å)	E_{coh} (eV per atom)	E_f (eV per atom)
3.002	2.21	1.94	5.64	−3.67	−1.23

group, as shown in Fig. 1(a) and (b). After full structural relaxation, the lattice parameters were $a = b = 3.002$ Å and are listed in Table 1 along with the nearest distances for Si–S and Si–O bonds and the effective thickness (h_{eff}).

To examine the dynamic stability of the Janus SiOS monolayer, we present the phonon spectrum in Fig. S1. The absence of any imaginary (negative) modes in the Brillouin zone confirms the dynamic stability of the system. Furthermore, a quadratic dispersion is observed in the flexural (ZA) mode near the Γ point, which is a characteristic of typical 2D materials.[45] To address the discrepancy observed in the acoustic phonon mode around the K point, we recalculated the phonon dispersion at finite temperatures ranging from 0 to 900 K by incorporating quartic anharmonic effects within SCPH. The resulting temperature-dependent phonon dispersions are shown in Fig. 1(c). Upon heating, the soft acoustic mode exhibits clear hardening, indicating that quartic anharmonicity stabilizes the lattice dynamics and significantly influences the thermal transport properties.

The mechanical properties were evaluated using the strain-energy method, in which small strains ranging from ±2% in steps of 0.5% were applied to extract the elastic constants.[46] Owing to the hexagonal symmetry, only two independent elastic constants were obtained, namely $C_{11} = 121.39$ N m^{-1} and $C_{12} = 58.99$ N m^{-1}. These values satisfy the Born stability criteria for a 2D hexagonal lattice ($C_{11} > 0$ and $|C_{12}| < C_{11}$),[47] thereby confirming the mechanical stability of the monolayer. Based on the calculated elastic constants, we further derived the orientation-dependent Young's modulus and Poisson's ratio and presented their polar plots using the corresponding formulas (Fig. S2).[48] Table S1 presents the calculated Young's modulus and Poisson's ratio of the studied Janus silicon oxysulfide monolayer, which exhibits a Young's modulus of 92.72 N m^{-1}, comparable to related 2D materials such as Si_2OSe (94 N m^{-1}) and Si_2OS (88.94 N m^{-1}).[49] Additionally, the corresponding polar plots show a circular shape, reflecting the directional isotropy of the monolayer (Fig. S2(a) and (b)).

Furthermore, we calculated the cohesive energy using the following formula:[50]

$$E_{coh} = \frac{E_{total} - E_{Si} - E_O - E_S}{N_{atoms}} \quad (3)$$

where E_{total} is the total energy of the monolayer, E_{Si}, E_O, and E_S are the energies of isolated silicon, oxygen, and sulfur atoms, respectively, and the computed value of E_{coh} is −3.67 eV per atom; this value lies within the typical range reported for other monolayers such as phosphorene (−3.46 eV per atom)[51] and SiS_2 (−3.51 eV per atom),[52] indicating the reliable experimental synthesizability and energetic stability of the Janus SiOS monolayer.

To assess the thermodynamic stability of the Janus monolayer, its formation energy was evaluated and compared with those of its parent SiS_2 and SiO_2 monolayers:[53]

$$E_f = E_{total} - \sum_i n\mu_i \quad (4)$$

where μ_i represents the chemical potential of the constituent elements taken from their stable elemental phases, and the computed E_f of the proposed Janus is −1.23 eV per atom, which lies between those of SiO_2 (−2.23 eV per atom) and SiS_2 (−0.66 eV per atom), indicating that SiOS is thermodynamically stable and does not dissociate into its parent monolayers.

To further assess the thermal effects, we carried out AIMD at 300 K. As shown in Fig. S3(a), the total energy remains nearly constant over time, and we also performed root-mean-square displacement (RMSD) analysis of the atomic trajectories in Fig. S3(b), which shows a rapid increase at the initial equilibration stage and then a slight thermal vibration of atoms around their equilibrium position, indicating minimal structural distortion and excellent thermal stability of the Janus.

Electronic properties

The calculated band structure shown in Fig. 2(a) indicates that the Janus SiOS monolayer is a direct bandgap semiconductor with a bandgap energy of 2.31 eV at the HSE06 level of theory. Such a wide bandgap may reduce the bipolar effect,[54] enhancing thermoelectric performance at higher temperatures. As shown in the figure, the valence band maximum (VBM) is mainly dominated by the S atom with a minor contribution from the O atom, whereas the conduction band minimum (CBM) is primarily governed by the Si atom with a moderate contribution from S. Furthermore, the projected density of states (PDOS) presented in Fig. 2(b) reveals that the VBM originates mainly from the Si-3p orbitals, while the Si-3s orbital dominates the CBM. We analyzed the bonding features of the Janus SiOS structure using crystal orbital Hamilton population (–COHP) analysis, which separates the electronic structure into

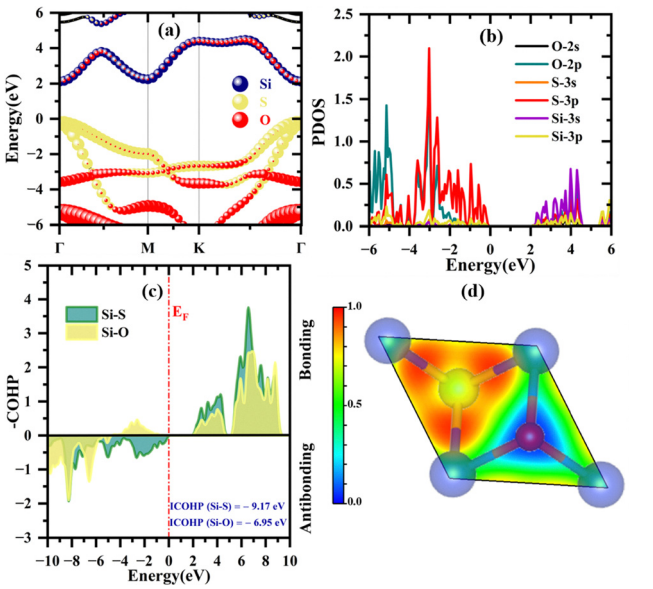

Fig. 2 Calculated (a) band structure, (b) projected density of states, (c) crystal orbital Hamilton population analysis (–COHP), and (d) electron localization function (ELF), where the blue-to-red color scheme indicates the low to high probability of electron localization around the atoms of the Janus SiOS monolayer.

bonding and antibonding contributions in the –COHP curves.[55] Our results, shown in Fig. 2(c), reveal that the antibonding states are located below the Fermi level, while strong Si–S bonding states appear above it. Furthermore, the integrated COHP (ICOHP) value for the Si–S bond is −9.17 eV, indicating a strong bonding interaction and enhanced structural stability of the Janus SiOS monolayer. The electron localization function (ELF) shown in Fig. 2(d) examines the chemical bonding characteristics, where the red regions indicate areas of high electron localization, corresponding to strong covalent bonds and polarity of this monolayer.

Lattice thermal conductivity

The lattice thermal conductivity is estimated by incorporating both intrinsic three- and four-phonon scattering processes and extrinsic mechanisms (isotope and boundary scattering) and using non-analytic corrections to enable dipole–dipole interactions. Thus, the lattice thermal conductivity is expressed as:[56]

$$\kappa_{\mathrm{ph}} = \frac{1}{V}\sum_{\lambda} C_{\lambda}\nu_{\lambda}^{2}\tau_{\lambda} \tag{5}$$

Here, C_λ, ν_λ, and τ_λ refer to the mode-specific heat, phonon group velocity, and phonon lifetime, respectively. According to Fig. 3(a), the temperature dependence of κ_{ph} shows a decrease as temperature increases, following the typical $1/T$ law.[57] The computed room temperature lattice thermal conductivity is 0.38 W mk^{-1} considering only three phonon scattering (3ph), which is significantly lower than that of the parents, two-dimensional hexagonal SiO_2 (∼12.5 W mk^{-1})[58] and SiS_2 (15.85 W mk^{-1}).[59] After incorporating the four-phonon scattering model (3ph + 4ph), the lattice thermal conductivity is significantly reduced to 0.186 W mk^{-1} at room temperature, corresponding to approximately 50% reduction and in good agreement with previous studies.[60] The contributions of the individual phonon modes (ZA, TA, LA, and optical modes) to the overall lattice thermal conductivity are illustrated in Fig. 3(b). Notably, the acoustic modes ZA, TA, and LA are the main contributors to the total κ_{ph}, and TA phonon modes take the most significant portion of the lattice thermal conductivity. Our results differ from those of typical 2D materials, where the ZA mode holds the majority contribution in pristine graphene due to mirror symmetry (selection rule).[61,62] This unusual finding can be attributed to the broken selection rule in our Janus monolayer.[63] Fig. 3(c) demonstrates that the acoustic branch accounts for 96.38% of $\kappa_{3\mathrm{ph}}$, while the optical branches contribute 3.62% across the full phonon frequency range. To provide a deeper understanding of size-dependent heat transport in the monolayer, we present the cumulative lattice thermal conductivity ($\kappa_{\mathrm{ph}}^{\mathrm{cumulative}}$) over the phonon mean free path (MFP) at 300 K. Fig. 3(d) illustrates that cumulative thermal conductivity increases with MFP until it reaches the thermodynamic limit. Furthermore, we introduce a simple parametric function to characterize the MFP, which represents the typical distance that phonons travel before scattering.[35]

$$\kappa_{\mathrm{ph}}^{\mathrm{cumulative}}(l \le l_{\max}) = \frac{\kappa_{\max}}{1+\frac{l_0}{l_{\max}}} \tag{6}$$

where $\kappa_{\max}$ refers to the saturated lattice thermal conductivity when all phonons are considered, $l_{\max}$ is the maximal MFP, and l_0 represents the characteristic MFP to be determined. The fitted curve shown in Fig. 3(d) indicates that the relevant heat transport MFP (l_0) in the Janus silicon oxy-sulfide monolayer is 350.45 nm, which corresponds to half of the total conductivity carried by phonons. This result provides a valuable physical summary for designing nanostructures intended for thermoelectric applications.

We next analyze the factors contributing to the suppressed lattice thermal conductivity observed in the Janus SiOS monolayer. Accordingly, we first present the phonon group velocity as a function of phonon frequency in Fig. 4(a), which demonstrates that the v_g of acoustic modes is lower than that of optical modes. The obtained average phonon group velocities for the acoustic (ZA, TA, and LA) and optical modes are 2.66, 1.97, 3.40, and 1.37 km s^{-1}, respectively. This trend is consistent with that reported for the SnS_2 monolayer and graphene.[64] Therefore, the moderate group velocity has a limited impact on lattice thermal conductivity. Instead, the ultralow κ_{ph} is attributed to strong anharmonic interactions within the crystal. To quantify the strength of anharmonicity, we show in Fig. 4(b) the mode dependent Grüneisen parameter as a function of phonon frequency. From the figure, we observed that the ZA mode exhibits a large γ, which contributes to the suppressed lattice thermal conductivity of the Janus SiOS monolayer. Fig. 4(c) and (d) depict the anharmonic phonon scattering rate and phonon lifetime of the Janus SiOS monolayer at room temperature. The Janus SiOS monolayer exhibits strong anharmonic phonon scattering at low frequencies. Meanwhile, most phonon modes exhibit short lifetimes of less than 10 ps, confirming that strong

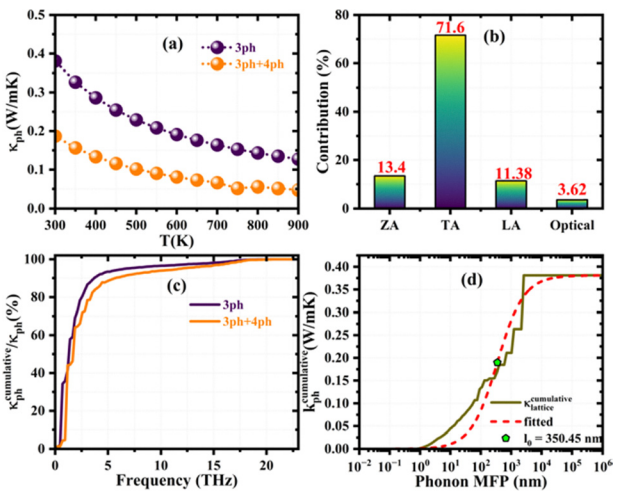

Fig. 3 Calculated (a) lattice thermal conductivity (κ_{ph}) including three- (3ph) and four-phonon (4ph); (b) contributions of different phonon modes (ZA, TA, LA, and Optical) to the overall lattice thermal conductivity; (c) and (d) accumulated phonon lattice thermal conductivity ($\kappa_{\mathrm{ph}}^{\mathrm{cumulative}}$) as a function of the phonon and MFP, with the dashed line presenting the fitting data of the Janus SiOS monolayer.

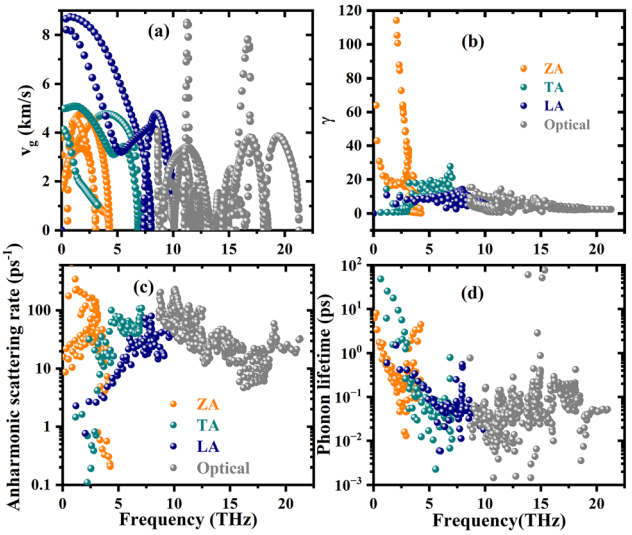

Fig. 4 Calculated (a) averaged phonon group velocity (v_g), (b) Grüneisen parameter (γ), (c) anharmonic scattering rate, and (d) phonon lifetime of the Janus SiOS monolayer.

anharmonic interactions dominate heat transport, which suppresses lattice thermal conductivity.

It is worth noting that previous studies have reported that coherent (wave-like) contributions to thermal transport can be significant in strongly anharmonic systems with ultralow lattice thermal conductivity.[65] The present Janus SiOS monolayer is characterized by strong anharmonicity associated with the soft ZA phonon branch. Thereby, coherent phonon transport in this system is expected to be important and cannot be accurately described within the Boltzmann transport framework employed in this work.[66]

Electronic transport properties

To accurately describe the electronic transport properties, we defined the total carrier relaxation time as the combination of the impurity scattering (τ_{IMP}), the acoustic deformation potential scattering (τ_{ADP}), and polar optical phonon scattering (τ_{POP}), mechanisms using the following expression:[32]

$$\frac{1}{\tau} = \frac{1}{\tau_{IMP}} + \frac{1}{\tau_{ADP}} + \frac{1}{\tau_{POP}} \quad (7)$$

The weighting of each mechanism was evaluated as a function of temperature and carrier concentration and illustrated in Fig. S6 and S7 for the n-type and p-type Janus SiOS monolayer, respectively. From Fig. S6(a), the ionized impurity scattering shows an apparent increase with carrier concentration because higher doping levels introduce more charged impurities that act as scattering centers. At the same time, the nearly constant behavior of acoustic deformation potential (Fig. S6(b)) and polar optical phonon scattering (Fig. S6(c)) with respect to charge carrier concentration indicates that these mechanisms are governed by phonon populations, which explain their increase with temperature and their remaining almost independent of carrier concentration. Fig. 5(a) and (b) present the calculated total carrier relaxation time for both the n-type and

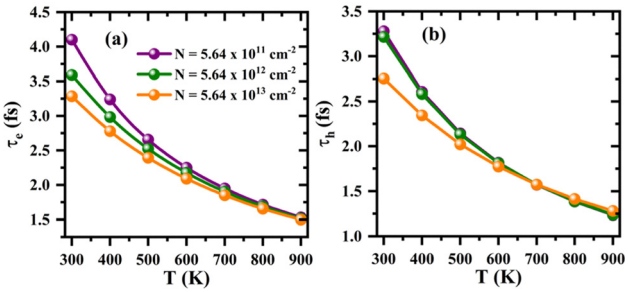

Fig. 5 Calculated total carrier relaxation time as a function of temperature at different carrier concentrations for (a) n-type and (b) p-type Janus SiOS monolayer.

p-type Janus SiOS monolayer. At room temperature, the n-type system exhibits a relatively higher relaxation time than the p-type Janus SiOS monolayer. For both carrier types, the relaxation time decreases with increasing temperature, which is consistent with the commonly reported temperature-dependent behavior of carrier relaxation times.[67]

Under the relaxation-time and rigid band approximations, the electrical conductivity (σ), Seebeck coefficient (S), and electronic thermal conductivity (κ_e) are derived from the solution of the linearized semiclassical Boltzmann transport equation in terms of the generalized transport coefficients:[29]

$$\mathcal{L}^{(m)}(\mu, T) = e^2 \int \sum(\varepsilon, T)\,(\varepsilon - \mu)^m \left(-\frac{\partial f_0(\varepsilon; \mu, T)}{\partial \varepsilon}\right) \mathrm{d}\varepsilon \quad (8)$$

where $\Sigma(\varepsilon, T)$ is the spectral conductivity, defined as

$$\sum(\varepsilon, T) = \sum(\varepsilon, T) = \frac{1}{V}\sum_k v_k^2\, \tau_k(T)\, \delta(\varepsilon - \varepsilon_k) \quad (9)$$

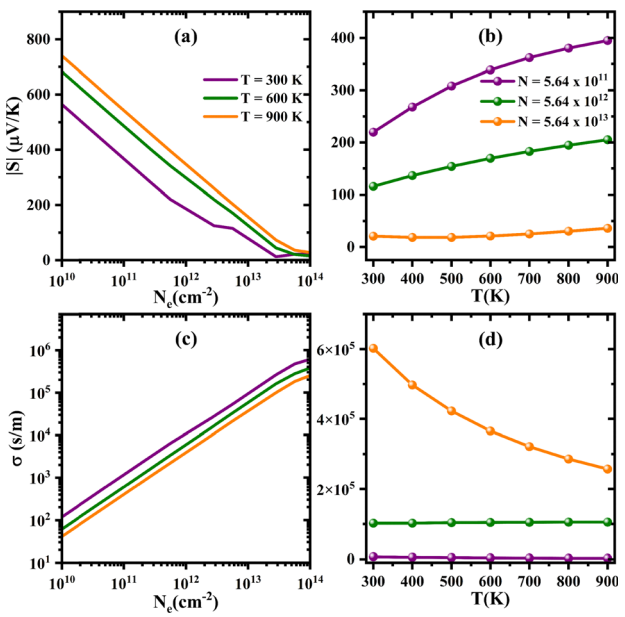

Fig. 6 Calculated absolute Seebeck coefficient (|S|) and electrical conductivity (σ) *versus* (a) and (c) carrier concentration (N_e) and (b) and (d) temperature (T) for the n-type Janus SiOS monolayer.

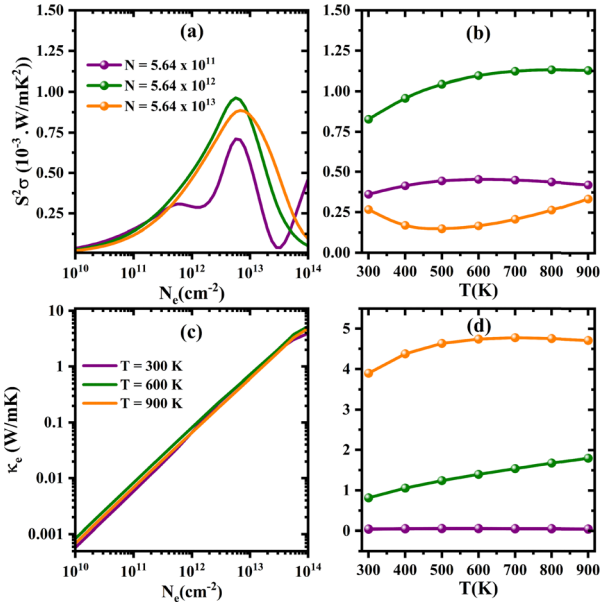

Fig. 7 Calculated power factor ($S^2\sigma$) and electronic thermal conductivity (κ_e) (a) and (c) *versus* carrier concentration (N_e) and (b) and (d) temperature (T) for the n-type Janus SiOS monolayer.

The electronic transport coefficients are then given by

$$S = -\frac{1}{qT}\frac{\mathcal{L}^{(1)}}{\mathcal{L}^{(0)}} \tag{10}$$

$$\sigma = \mathcal{L}^{(0)} \tag{11}$$

$$\kappa_e = \frac{1}{e^2 T}\left[\frac{\left(\mathcal{L}^{1}\right)^2}{\mathcal{L}^{0}} - \mathcal{L}^{2}\right] \tag{12}$$

Fig. 6(a) and (b) show the absolute Seebeck coefficient ($|S|$) of the n-type Janus SiOS monolayer over the temperature range of 300–900 K at different carrier concentrations, while the corresponding results for the p-type system are presented in Fig. S8. The absolute Seebeck coefficient decreases with increasing carrier concentration, whereas it increases approximately linearly with temperature over the moderate temperature range. The obtained $|S|$ values corresponding to the optimal thermoelectric performance are 394.5 μV K^{-1} for the n-type and 378.5 μV K^{-1} for the p-type at 900 K and at a carrier concentration of 3.64 × 10^{11} cm^{-2}, which are comparable to those reported for common 2D thermoelectric materials.[68–70] By incorporating the calculated relaxation time, the n-type electrical conductivity for the Janus monolayer system is evaluated. Fig. 6(c) and (d) present the variation of electrical conductivity over carrier concentration and temperature, showing a trend opposite to that of the Seebeck coefficient, with a notable increase with carrier concentration, while the temperature dependence of σ remains negligible at low doping levels. It is worth noting that the larger n-type relaxation time leads to a higher n-type electrical conductivity than that of the p-type doping (Fig. S8).

Fig. 7(a) and (b) show the computed thermoelectric power factor (PF) for the n-type Janus SiOS monolayer as a function of carrier concentration and temperature. The peak power factor was found to be 0.87 × 10^{-3} W mK^{-2} at 5.64 × 10^{12} cm^{-2}, showing a good agreement with earlier studies on two-dimensional thermoelectric monolayers, such as p-type In_2SeTe (0.63 × 10^{-3} W mK^{-2}),[71] n-type BiTeSe (0.14 × 10^{-3} W mK^{-2}),[72] n-type γ-Ge_2SSe (2.6 × 10^{-3} W mK^{-2}),[73] and p-type SnSSe (2.8 × 10^{-3} W mK^{-2}).[74] We then computed the electronic thermal conductivity (κ_e). As shown in Fig. 7(c) and (d), κ_e increases with rising carrier concentration because more charge carriers participate in the transport of heat. This trend follows the Wiedemann–Franz law.[75] The electronic thermal conductivity calculated directly from the Boltzmann transport equation agreed with that estimated using the Wiedemann–Franz formalism (refer to Fig. S10).

Thermoelectric power efficiency

Coupling the ultralow lattice thermal conductivity ($\kappa_{3ph+4ph}$) and considering electron–phonon scattering, we can accurately predict ZT of the Janus SiOS monolayer. This monolayer shows promising optimal ZT values of 3.62 and 2.7 at 900 K and 5.64 × 10^{11} cm^{-2} for n-type and p-type doping, respectively (Fig. 8(a) and (b)). Our predicted figure merit was promising as compared to other typical monolayers such as PbTe (1.55 at 900 K),[76]

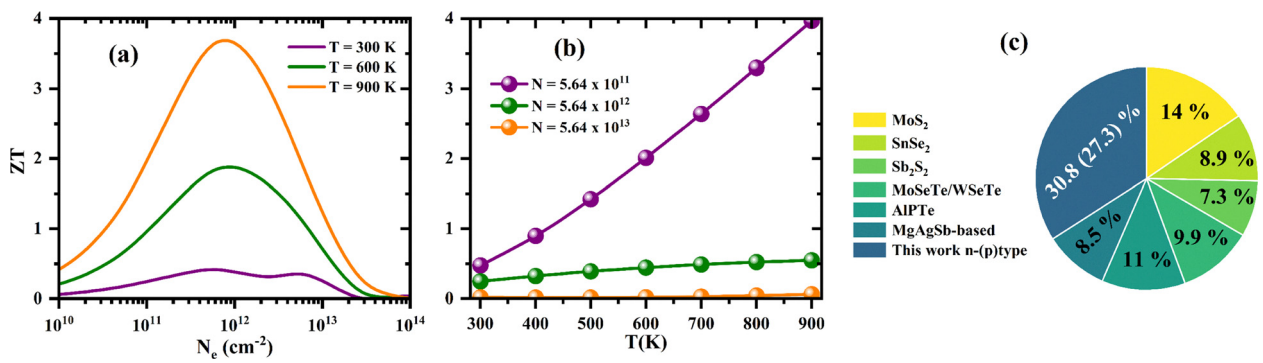

Fig. 8 Calculated figure of merit (ZT) *versus* (a) carrier concentration (N_e) and (b) temperature (T) for the n-type Janus SiOS monolayer; (c) comparison of the thermoelectric conversion efficiency (η(%)) between typical thermoelectric materials, such as MoS_2,[82] SnSe,[83] MoSeTe/WSeTe,[84] Sb_2S_2Te,[85] AlPTe,[86] and MgAgSb-based,[87] and this work.

T-SnSSe (1.75 at 900),[68] Re_6Se_8I (1.45 at 900 K),[77] and SiS (1.99 at 700 K),[78] and larger than its parent SiS_2 (0.77 at 900 K).[59,79] Since *ZT* is a material descriptor, we computed the maximum conversion efficiency η to bridge the gap between material properties and device performance, thereby assessing the suitability of this monolayer for practical applications (eqn (1)).[80] Here we set T_{cold} = 300 K, T_{hot} = 900 K, and $\overline{ZT} = \int_{T_{cold}}^{T_{hot}} ZT\,dT / T_{hot} - T_{cold}$.[81] The calculations show that the n-type and p-type Janus SiOS monolayers exhibit thermoelectric efficiencies of 30.89% and 27.32%, respectively, which are higher than those of a set of documented promising thermoelectrics (Fig. 8(c)).

Conclusion

We systematically analyzed the electronic, thermal, and transport properties of the Janus SiOS monolayer using DFT, coupled with solving the BTE for electrons and phonons, while considering three main scattering mechanisms (ADP, POP, and IMP). The results show excellent dynamic, thermal, mechanical, and energetic stability, along with a tunable band gap and strong covalent bonds in the Janus SiOS monolayer. The higher anharmonic scattering rate, significant Grüneisen parameter, short phonon lifetime, moderate phonon group velocity, broken selection rules, and four-phonon scattering contribute to an ultralow lattice thermal conductivity. Additionally, the wider band gap reduces the bipolar effect at 900 K, enhancing the Seebeck coefficient and power factor. Consequently, a maximum *ZT* value of 3.62 is achieved at 900 K for the n-type SiOS monolayer, indicating a promising thermoelectric efficiency of 30.8%. These combined properties suggest that the Janus SiOS monolayer is a viable candidate for waste heat recovery applications.

Author contributions

All authors contributed to the data analysis and improvement of the manuscript. Zakariae Darhi performed all calculations and prepared the original draft. Mounaim Bencheikh, Ravindra Pandey, and Larbi El Farh reviewed and edited the manuscript and approved the final version for publication.

Conflicts of interest

There are no conflicts to declare.

Data availability

The data supporting the findings of this study are available within the article and its supplementary information (SI). Supplementary information is available. See DOI: https://doi.org/10.1039/d5ma01306b.

Acknowledgements

The authors sincerely thank S. Gowtham and acknowledge the computational resources provided by Michigan Technological University.

References

1 D. F. Birol, World Energy Outlook 2024, 2024.
2 C. Forman, I. K. Muritala, R. Pardemann and B. Meyer, *Renewable Sustainable Energy Rev.*, 2016, **57**, 1568–1579.
3 Z. Darhi, A. Rawat, R. Pandey and L. Elfarh, *Mater. Sci. Semicond. Process.*, 2025, **185**, 108896.
4 C. Gayner and K. K. Kar, *Prog. Mater. Sci.*, 2016, **83**, 330–382.
5 H. S. Kim, W. Liu, G. Chen, C.-W. Chu and Z. Ren, *Proc. Natl. Acad. Sci. U. S. A.*, 2015, **112**, 8205–8210.
6 W.-J. Yin, H.-J. Tan, P.-J. Ding, B. Wen, X.-B. Li, G. Teobaldi and L.-M. Liu, *Mater. Adv.*, 2021, **2**, 7543–7558.
7 K. S. Novoselov, A. K. Geim, S. V. Morozov, D.-E. Jiang, Y. Zhang, S. V. Dubonos, I. V. Grigorieva and A. A. Firsov, *Science*, 2004, **306**, 666–669.
8 C. Jin, X. Tang, X. Tan, S. C. Smith, Y. Dai and L. Kou, *J. Mater. Chem. A*, 2019, **7**, 1099–1106.
9 W. Ahmad, Y. Wang, J. Kazmi, U. Younis, N. M. Mubarak, S. H. Aleithan, A. I. Channa, W. Lei and Z. Wang, *Laser Photon. Rev.*, 2025, **19**, 2400341.
10 M. Bencheikh, L. El Farh, S. Malki, Z. Darhi, I. Guesmi, A. Challioui and S. Kaya, *J. Opt.*, 2025, **54**, 1140–1148.
11 A. Patel, D. Singh, Y. Sonvane, P. Thakor and R. Ahuja, *ACS Appl. Mater. Interfaces*, 2020, **12**, 46212–46219.
12 Z. Darhi, L. El Farh, R. Pandey, I. Guesmi and S. Malki, *Surf. Interfaces*, 2025, 107385.
13 Z. Darhi, L. El Farh and R. Pandey, *Materials*, 2025, **18**, 294.
14 M. Bencheikh and Z. Darhi, *Solid State Commun.*, 2025, 116150.
15 Y. Zhao, B. Zhang and J. Lin, *Appl. Surf. Sci.*, 2023, **621**, 156883.
16 R. Gupta, B. Dongre, C. Bera and J. S. Carrete, *J. Phys. Chem. C*, 2020, **124**, 17476–17484.
17 L. Pan, Z. Wang, J. Carrete and G. K. Madsen, *Phys. Rev. Mater.*, 2022, **6**, 084005.
18 S.-D. Guo and Phys Chem, *Chem. Phys.*, 2018, **20**, 7236–7242.
19 X. Yan, X. Cui, B. Wang, H. Yan, Y. Cai and Q. Ke, *iscience*, 2023, **26**(5), 106731.
20 C. Büchner, Z.-J. Wang, K. M. Burson, M.-G. Willinger, M. Heyde, R. Schlögl and H.-J. Freund, *ACS Nano*, 2016, **10**, 7982–7989.
21 T. DiStefano and M. Shatzkes, *J. Vac. Sci. Technol.*, 1976, **13**, 50–54.
22 R. O. Suzuki, Y. Yashima, T. Kaneko, E. Ahmadi, T. Kikuchi, T. Watanabe and G. Nogami, *Metall. Mater. Trans. B*, 2021, **52**, 1379–1391.
23 M.-X. Xie, J.-W. Zhang, Y. Zhang, H.-R. Wu, Y.-P. Wang, W.-H. Wang and G.-Q. Shao, *ACS Omega*, 2022, **7**, 22500–22510.

24 K.-H. Nam, D.-H. Kim, Y.-H. Lee, S. C. Han, J.-H. Choi, Y.-C. Ha and C.-M. Park, *J. Mater. Chem. A*, 2023, **11**, 4987–5000.
25 J. Hafner, *J. Comput. Chem.*, 2008, **29**, 2044–2078.
26 J. P. Perdew, K. Burke and M. Ernzerhof, *Phys. Rev. Lett.*, 1996, **77**, 3865.
27 H. J. Monkhorst and J. D. Pack, *Phys. Rev. B*, 1976, **13**, 5188.
28 S. Grimme, J. Antony, S. Ehrlich and H. Krieg, *J. Chem. Phys.*, 2010, **132**, 154104.
29 G. K. Madsen, J. Carrete and M. J. Verstraete, *Comput. Phys. Commun.*, 2018, **231**, 140–145.
30 J. Heyd and G. E. Scuseria, *J. Chem. Phys.*, 2004, **121**, 1187–1192.
31 A. M. Ganose, J. Park, A. Faghaninia, R. Woods-Robinson, K. A. Persson and A. Jain, *Nat. Commun.*, 2021, **12**, 2222.
32 G. Casu, A. Bosin and V. Fiorentini, *Phys. Rev. Mater.*, 2020, **4**, 075404.
33 M. Bernardi, *Eur. Phys. J. B*, 2016, **89**, 239.
34 F. Giustino, *Rev. Mod. Phys.*, 2017, **89**, 015003.
35 W. Li, J. Carrete, N. A. Katcho and N. Mingo, *Comput. Phys. Commun.*, 2014, **185**, 1747–1758.
36 Z. Han, X. Yang, W. Li, T. Feng and X. Ruan, *Comput. Phys. Commun.*, 2022, **270**, 108179.
37 S. Baroni, S. De Gironcoli, A. Dal Corso and P. Giannozzi, *Rev. Mod. Phys.*, 2001, **73**, 515.
38 A. Togo, *J. Phys. Soc. Jpn.*, 2023, **92**, 012001.
39 T. Tadano, Y. Gohda and S. Tsuneyuki, *J. Phys.: Condens. Matter*, 2014, **26**, 225402.
40 F. Eriksson, E. Fransson and P. Erhart, *Adv. Theory Simul.*, 2019, **2**, 1800184.
41 Z. Tang, X. Wang, C. He, J. Li, M. Chen, C. Tang and T. Ouyang, *Phys. Rev. B*, 2024, **110**, 134320.
42 W. G. Hoover, *Phys. Rev. A:At., Mol., Opt. Phys.*, 1985, **31**, 1695.
43 S. Nosé, *J. Chem. Phys.*, 1984, **81**, 511–519.
44 X. Wu, V. Varshney, J. Lee, Y. Pang, A. K. Roy and T. Luo, *Chem. Phys. Lett.*, 2017, **669**, 233–237.
45 A. Taheri, S. Pisana and C. V. Singh, *Phys. Rev. B*, 2021, **103**, 235426.
46 R. Golesorkhtabar, P. Pavone, J. Spitaler, P. Puschnig and C. Draxl, *Comput. Phys. Commun.*, 2013, **184**, 1861–1873.
47 F. Mouhat and F.-X. Coudert, *Phys. Rev. B:Condens. Matter Mater. Phys.*, 2014, **90**, 224104.
48 W. Xiong, K. Huang and S. Yuan, *J. Mater. Chem. C*, 2019, **7**, 13518–13525.
49 N. P. Anh, N. Poklonski, V. T. Vi, C. Q. Nguyen and N. N. Hieu, *RSC Adv.*, 2024, **14**, 4966–4974.
50 M. A. Mohebpour, S. M. Mozvashi, S. I. Vishkayi and M. B. Tagani, *Sci. Rep.*, 2020, **10**, 14963.
51 J. Ahn, I. Hong, Y. Kwon, R. C. Clay, L. Shulenburger, H. Shin and A. Benali, *Phys. Rev. B*, 2018, **98**, 085429.
52 Z. Huang, K. Ren, R. Zheng, L. Wang and L. Wang, *Molecules*, 2023, **28**, 4126.
53 S. Zhang and J. E. Northrup, *Phys. Rev. Lett.*, 1991, **67**, 2339.
54 W. H. Shin, H.-S. Kim, S. Y. Kim, S.-S. Choo, S.-W. Hong, Y. Oh, Y. Yang, Y. Kim, H. J. Park and S.-I. Kim, *Energies*, 2020, **13**, 337.
55 R. Nelson, C. Ertural, J. George, V. L. Deringer, G. Hautier and R. Dronskowski, *J. Comput. Chem.*, 2020, **41**, 1931–1940.
56 R. Tan, K. Zhang and Y.-W. Fang, *arXiv*, 2025, preprint, arXiv:2507.21734, DOI: 10.48550/arXiv.2507.21734.
57 B. Peng, H. Zhang, H. Shao, Y. Xu, X. Zhang and H. Zhu, *Sci. Rep.*, 2016, **6**, 20225.
58 Y. Wang, Z. Song and Z. Xu, *Phys. Rev. B:Condens. Matter Mater. Phys.*, 2015, **92**, 245427.
59 J. Bera, A. Betal, Z. Singh, A. N. Gandi and S. Sahu, *Comput. Mater. Sci.*, 2022, **201**, 110931.
60 Z. Tang, X. Wang, J. Li, C. He, M. Chen, C. Tang and T. Ouyang, *Phys. Rev. B*, 2023, **108**, 214304.
61 L. Lindsay, D. Broido and N. Mingo, *Phys. Rev. B:Condens. Matter Mater. Phys.*, 2010, **82**, 115427.
62 L. Lindsay, W. Li, J. Carrete, N. Mingo, D. Broido and T. Reinecke, *Phys. Rev. B:Condens. Matter Mater. Phys.*, 2014, **89**, 155426.
63 G. Liu, H. Wang, Z. Gao and G.-L. Li, *Phys. Chem. Chem. Phys.*, 2020, **22**, 16796–16803.
64 S. Karak, J. Bera, S. Paul, S. Sahu and S. Saha, *Phys. Rev. B*, 2021, **104**, 195304.
65 M. Simoncelli, N. Marzari and F. Mauri, *Nat. Phys.*, 2019, **15**, 809–813.
66 A. Minnich, *J. Phys.: Condens. Matter*, 2015, **27**, 053202.
67 H. Huang, X. Fan, D. J. Singh and W. Zheng, *J. Mater. Chem. C*, 2020, **8**, 9763–9774.
68 S. Tang, S. Bai, M. Wu, D. Luo, J. Zhang, D. Wang, S. Yang and L.-D. Zhao, *Mater. Today Phys.*, 2022, **29**, 100923.
69 Y.-Q. Lin, Q. Yang, Z.-Q. Wang, H.-Y. Geng and Y. Cheng, *Phys. Chem. Chem. Phys.*, 2023, **25**, 31312–31325.
70 W.-L. Tao, J.-Q. Lan, C.-E. Hu, Y. Cheng, J. Zhu and H.-Y. Geng, *J. Appl. Phys.*, 2020, 127.
71 R. Xiong, W. Li, Y. Zhang, Z. Cui, C. Wen, M. Anpo, B. Wu and B. Sa, *J. Mater. Chem. C*, 2022, **10**, 10480–10490.
72 K. Sujata, N. Verma, R. G. Solanki and A. Kumar, *Mater. Adv.*, 2025, **6**, 849–859.
73 V. J. Ramirez Rivera, F. Mamani Gonzalo, H. E. Nina Mendoza, M. Jeomar Piotrowski, J. A. Chacaltana Garcia, E. Rodrigues Delgado and E. Mamani Flores, *J. Appl. Phys.*, 2024, **136**, 234301.
74 H. Nautiyal and P. Scardi, *Nanotechnology*, 2022, **33**, 325402.
75 H.-S. Kim, Z. M. Gibbs, Y. Tang, H. Wang and G. J. Snyder, *APL Mater.*, 2015, **3**, 041506.
76 S. Tang, M. Wu, S. Bai, D. Luo, J. Zhang and S. Yang, *J. Alloys Compd.*, 2022, **907**, 164439.
77 T. Li, P.-H. Du, L. Bai, Q. Sun and P. Jena, *Phys. Rev. Appl.*, 2022, **18**, 064067.
78 J.-H. Yang, Q. Yuan, H. Deng, S.-H. Wei and B. I. Yakobson, *J. Phys. Chem. C*, 2017, **121**, 123–128.
79 M. Naseri, M. Abutalib, M. Alkhambashi, J. Gu, J. Jalilian, A. Farouk and J. Batle, *Phys. E*, 2019, **114**, 113581.
80 G. J. Snyder and E. S. Toberer, *Nat. Mater.*, 2008, **7**, 105–114.
81 Y. Luo, S. Cai, X. Hua, H. Chen, Q. Liang, C. Du, Y. Zheng, J. Shen, J. Xu and C. Wolverton, *Adv. Energy Mater.*, 2019, **9**, 1803072.

82 S. S. Nair and N. Singh, *Mater. Today NANO*, 2025, **29**, 100561.
83 B. Qin, D. Wang, T. Hong, Y. Wang, D. Liu, Z. Wang, X. Gao, Z.-H. Ge and L.-D. Zhao, *Nat. Commun.*, 2023, **14**, 1366.
84 C. Wang, Y.-X. Chen, G. Gao, K. Xu and H. Shao, *Appl. Surf. Sci.*, 2022, **593**, 153402.
85 X. Liu, S. Yuan, B. Gu, Q. Chen, X. Pu and J. Zhang, *Curr. Appl. Phys.*, 2022, **36**, 117–130.
86 M. Jakhar, A. Kumar and R. Pandey, *J. Phys. Chem. C*, 2023, **127**, 21465–21473.
87 D. Kraemer, J. Sui, K. McEnaney, H. Zhao, Q. Jie, Z. Ren and G. Chen, *Energy Environ. Sci.*, 2015, **8**, 1299–1308.